Diffuse Back-Illumination Extinction Imaging of Soot Formation from a Liquid Fuel Film

Chaoxu Chen[1,*], Yaoting Li[1], Fujio Akagi[1], Yannis Hardalupas[1], Alex M.K.P. Taylor[1]
1: Dept. of Mechanical Engineering, Imperial College London, UK
* Correspondent author: c.chen16@imperial.ac.uk

Keywords: DBIEI, Soot, Fuel film combustion, Ambient pressure, Oxygen Content

ABSTRACT

The transient combustion of a liquid iso-octane film, isolated from the often co-existing combustion of liquid sprays, was investigated within the nominally quiescent ambient of a constant volume chamber using a custom-made liquid fuel film generation system. Soot formation throughout the combustion process, from ignition to extinction, was visualized using high-speed diffuse back-illumination extinction imaging technique, providing temporally resolved spatial distribution of soot optical thickness (KL) in the chamber. The impact of ambient pressure and ambient oxygen content on soot formation was examined over a range of 2 – 5 bar (absolute) and 16 – 30% (in terms of molar fraction of oxygen), respectively. Regardless of the test conditions, the fuel film combustion entailed three stages, namely flame initiation, steady burning and flame extinction. While the ambient oxygen content was kept constant, the flame gradually became turbulent-like and the flame flickering less distinct as ambient pressure was increased. The total amount of soot generated within the chamber was found to first increase then decrease with the ambient pressure, due to the competing impacts of increasing pressure on promoting soot-formation reaction rate and enhancing mixing of fuel vapour with the entrained air. Increasing ambient oxygen content, on the other hand, consistently enhanced soot formation, which may be associated with its impact on boosting flame temperature and consequently liquid fuel evaporation rate. In addition, flame flickering remained distinct for ambient oxygen content above atmospheric level, while becoming substantially less observable for that below atmospheric level. Flickering frequency, for all test conditions with distinct flame flickering, had a value of approximately 10 Hz and gradually increased with time during the steady burning stage, suggesting the shrinkage of the fuel film diameter. Flickering of the flame resulted in fluctuations in the total amount of soot presented in the combustion chamber. The power of this fluctuation varied with time, and this temporal variation of fluctuation power also depended on experimental conditions, due to its dependency on the combined effects of soot concentration and volume of the flame.

1. Introduction

Gasoline direct injection (GDI) engines have seen a rapid growth in market share due to their improved engine performance and fuel economy compared to conventional port fuel injection engines (F. Zhao *et al.*, 1999; H. Zhao, 2010). In GDI engines, particularly at low load, fuel is often injected during the compression stroke when the piston is close to top dead centre, which can induce the formation of liquid fuel films on the piston surface, as a result of fuel impingement and

wall wetting (Ding *et al.*, 2018; He *et al.*, 2019; Karlsson & Heywood, 2001). After spark ignition, these fuel films may be ignited by the propagating flame, leading to pool fires and consequently undesirable soot production (Drake *et al.*, 2003; Miyashita *et al.*, 2016). Therefore, understanding the soot formation process during combustion of fuel films may lead to ways to reduce soot emission from GDI engines and thereby satisfy the increasingly stringent emission regulations.

To characterise soot formation during combustion of fuel films, Roque *et al.* (2019 a; 2019 b) and Chung *et al.* (2021) used a GDI injector to generate a fuel film on a metal plate placed within a constant volume chamber, while Jüngst and Kaiser (2019, 2021) generated fuel films on the wall of a constant-flow duct using a GDI injector. Although the fuel film generation mechanism in these studies closely resembles that in a real engine, it is difficult to isolate the combustion of the fuel films from the simultaneous combustion of – and soot generation by – the evaporating fuel sprays. In addition, the shot-to-shot variation of the liquid film formed by the GDI spray may be substantial (Duke *et al.*, 2016), which influences the soot formation physics.

To circumvent these two issues, this study utilised a custom-made fuel film generation system, which avoids the use of a fuel spray from a GDI injector; details of this system are presented under the section on experimental method. The fuel film was generated on a metal surface, and its combustion, initiated by a laser-induced spark, was enclosed in a constant volume chamber. Soot formation during combustion can be visualized and quantified in a temporally and spatially resolved manner with high-speed diffuse back-illumination extinction imaging (DBIEI) technique. DBIEI is an extinction-based, line-of-sight technique, which can provide two-dimensional information of soot optical thickness KL - product of the dimensional extinction coefficient K and the path length L through the particle cloud. Due to its ability to abate undesirable beam steering effects and therefore to improve the accuracy of KL measurement, DBIEI has been used to characterise soot formation during combustion of diesel sprays (Bjørgen *et al.*, 2019; Lind *et al.*, 2018; Westlye *et al.*, 2017). The light extinction due to soot particles present in the light path can be described using the Beer-Lambert law:

$$\frac{I_t}{I_0} = e^{-KL} \tag{1}$$

where I_0 is the incident light intensity and I_t the transmitted light intensity. However, when a flame is present in the light path, I_t cannot be directly measured due to the superposition of the flame's natural luminosity. This is generally solved by pulsing the illumination source and recording another image without illumination shortly before or after recording the image with illumination; here, the light intensity recorded *with* illumination is denoted as I and that *without* illumination as I_f. In addition, the incident light intensity often needs to be corrected for the

ambient background intensity, I_{BG}, which is recorded without flame and illumination. Consequently, equation (1) becomes:

$$\frac{I - I_f}{I_0 - I_{BG}} = e^{-KL} \tag{2}$$

In this study, iso-octane fuel films were combusted within an ambient atmosphere made up of a range of mixtures of nitrogen and oxygen. The influence of ambient pressure (P) and ambient oxygen content (in terms of molar fraction of oxygen, χ_{O_2}) on soot formation was characterised using DBIEI. The results not only help to better understand the combustion process of fuel films, but also provide a data set that can be used to evaluate numerical models of soot formation during fuel film combustion.

2. Experimental method

2.1. Experimental setup and test conditions

Fig. 1(a) schematically shows a plan view of the experimental setup, which primarily consists of four sub-systems, namely a constant volume chamber referred to as the Combustion Research Unit (CRU), a fuel-film generation system, the laser ignition system and the DBIEI system.

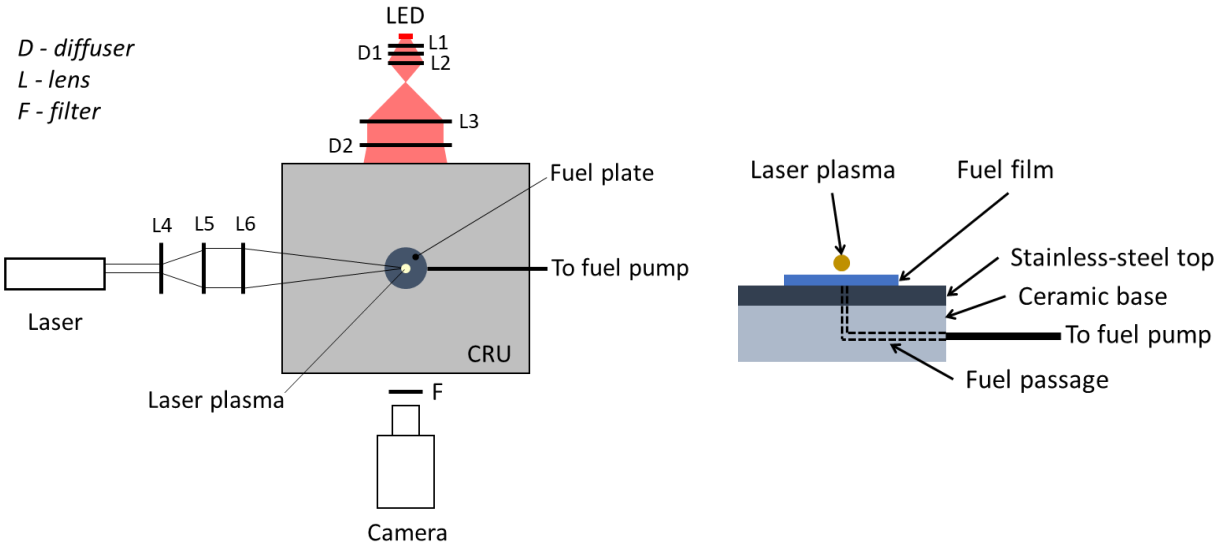

(a) Plan view of experimental setup (b) Elevation view of fuel plate

Fig. 1 Schematics of experimental setup

The CRU is a cuboidal chamber, with a volume of approximately 1.5 L and a maximum working pressure of 150 bar. Three Fused Silica windows with a diameter of 125 mm were fitted into frames

set into the walls of three faces of the cuboid, providing optical access for LED illumination, laser ignition and camera imaging respectively, as shown in Fig. 1(a). Four electrical heaters integrated in the CRU walls enabled control of the wall – and hence optical window – temperature ranging from room temperature to about 200 °C. The CRU wall temperature was set at 50 °C in this study to avoid condensation of combustion-produced water vapour on the inner surface of the optical windows. A gas port on the bottom wall of the CRU was connected to compressed Nitrogen and Oxygen pipelines via Mass Flow Controllers (MFC, Bronkhorst), which allowed filling the CRU to a target pressure with a user-specified N_2/O_2 mixture; the pressure within the CRU was monitored by a pressure sensor (PWF-10MPA, Tokyo Measuring Instruments Lab). Pressurized gas mixtures in the CRU could be released through another gas port on the bottom wall to a purge pipeline, which was connected to the atmosphere. More details about the CRU can be found in (Hua, 2021).
The main components of the fuel film generation system include a fuel plate and a fuel pump. The fuel plate, shown in elevation view in Fig. 1(b), had a diameter of 30 mm and was composed of a stainless-steel top (2 mm thick) and a ceramic base (12 mm thick); the ceramic base housed an electrical heater (HT19R, Thorlabs), which had a nominal power of 19 W and provided active control of the plate temperature. The fuel plate had a small 1 mm diameter central hole, which was connected to the fuel pump through the fuel passage shown in Fig. 1(b) and fuel pipes. When the fuel pump was activated, liquid fuel was released onto the fuel plate through the small hole which subsequently spread to form a fuel film. The fuel pump comprised a syringe and a syringe pump (Legato 100, Kd Scientific), which controlled the volumetric flow rate and duration of the fuel flow, and therefore the total volume of liquid fuel in the film. In this study, the fuel film was generated with 30 μL of iso-octane (technical grade, VWR), which was pumped onto the fuel plate at a fixed rate of 15 μL/s. The fuel film formed an approximately round 'puddle' with a diameter of about 15 mm, which corresponded to an average film thickness of 170 μm, assuming that the fuel film was a disk. The fuel film generation system was integrated into the CRU, so that the fuel plate was located as close to the centre of the bottom wall of the CRU as possible, thereby maximizing the available space above the plate to accommodate the flame from the fuel film.
Laser-induced spark ignition was adopted in this study to initiate the combustion of the fuel films in the sealed CRU. A laser-induced spark, generated by focusing a high-power laser beam, has proven to be a feasible and convenient ignition source (Phuoc, 2006; Ronney, 1994); the ignition mechanism, however, is beyond the scope of this study and therefore not discussed here. A 532 nm Q-switched Nd:YAG laser (Nano T, Litron Lasers), with a pulse duration of about 8 ns and pulse energy of about 120 mJ, was used to generate the ignition spark. The laser beam was expanded to approximately 20 mm in diameter by combining a diverging lens (L4 in Fig. 1(a),

LC1715-A, Thorlabs) and a focusing lens (L5 in Fig. 1(a), LBF254-150-A, Thorlabs), before being focused by another lens (L6 in Fig. 1(a), LA1708-A, Thorlabs) to a narrow waist. The ignition spark was located about 1 mm above the centre of the fuel film plate. The selected pulse energy and location of the ignition spark provided reliable ignition of the fuel film with a single laser pulse under the test conditions considered in this study.

The DBIEI system used in this study is modelled closely on the one reported by Westlye *et al.* (2017). A multi-die LED (dominant wavelength of 623 nm, LZP-04MD00, LED Engin), controlled by an in-house built driving unit, was able to deliver high optical output in pulses, with pulse duration down to approximately 0.5 μs and frequency up to about 100 kHz. In the present study, the LED was operated at 5 kHz with a pulse duration of 5 μs. The light output from the LED was collected by a condenser lens (L1 in Fig. 1(a), ACL25416U, Thorlabs), passed through a diffuser (D1 in Fig. 1(a), ED1-S20, Thorlabs) to improve its uniformity, and then focused by another condenser lens (L2 in Fig. 1(a), ACL25416U, Thorlabs). The diverging beam after the focal point was then collimated by a Fresnel lens (L3 in Fig. 1(a)) with diameter of 100 mm and focal length of 100 mm, and finally directed to a 100 mm diameter engineered diffuser (D2 in Fig. 1(a), EDC-15-15132, RPC Photonics); the output from the engineered diffuser was delivered into the CRU through one of the optical windows, providing an extended Lambertian illumination source with a divergence angle of approximately 18°. The engineered diffuser was placed about 195 mm away from the focal plane of the imaging camera, which coincided with the vertical axis of the fuel plate. A highspeed camera (FASTCAM SA1.1, Photron), fitted with a 50 mm Nikkor f/1.4 lens and a 500 mm close-up lens, was used to collect the transmitted LED light through the optical window on the opposite side of the CRU. The camera was triggered to record a pair of images every 2 ms; the two images had a time interval of 100 μs and an exposure time of 5.46 μs. The camera was synchronized to the LED such that every pair of captured images include one with LED illumination and the other without, which is required for the evaluation of KL, as discussed in the previous section. The timing of the camera was configured in this way such that the low overall recording frequency (500 Hz) allowed capturing the whole combustion process of the fuel film, while the short time interval in each pair of images ensured the imaging of an essentially 'frozen' flow field. The camera had a resolution of 768 x 768 pixels, resulting in a 73.7 x 73.7 mm^2 field of view. To minimize the flame luminosity captured by the camera while maximizing the captured LED illumination, a bandpass optical filter with a centre wavelength of 630 nm and FWHM of 10 nm (FB630-10, Thorlabs), and a neutral density filter with appropriate optical density, were fitted to the camera lens.

For each experimental test, the CRU, with an initial pressure of 1 atm, was first flushed three times

with pure N_2, regardless of the preceding gas contents. For each flush sequence, the CRU was first charged with N_2 until the pressure reached about 5 bar absolute; then the contents were left to mix for 2 minutes with the aid of a fan installed on the bottom wall of the CRU, before being released to the purge line until the absolute pressure dropped back to 1 atm. This process ensured that the gas remaining in the CRU after three flushes was almost pure N_2, with a volume fraction greater than 99%. A certain predetermined amount of N_2 and O_2, based on the target gas pressure and composition as listed in Table 1, was then charged into the CRU; note that 1 atm of N_2 already existed in the CRU before charging. It is also worth noting that for all test conditions listed in Table 1, the amount of oxygen charged into the CRU was at least 10 times more than the amount required for the complete combustion of the iso-octane fuel film. The charged gas was also left to mix for 2 minutes with the mixing fan in operation. The mixing fan was then stopped, before the liquid fuel pump was activated for 2 s to generate the fuel film. Laser ignition (single pulse) was initiated 0.5 s after the fuel pump stopped, allowing the fuel film to stabilize, and the camera recording was triggered at the end of the laser ignition pulse and continued for 9.7 s until the camera memory was full. After two flushes of the CRU, information of I_0 and I_{BG} were obtained by recording 100 images with LED illumination and 100 images without respectively; ensemble averages of these images were used as I_0 and I_{BG} in equation (2) for calculation of KL factor.

Table 1 summarizes test conditions examined in the present study, among which tests 1 – 4 examined the impact of ambient pressure on soot formation during fuel film combustion, while tests 2 and 5 – 7 examined the impact of ambient oxygen content. Measurement was repeated 5 times for each test condition.

Table 1 Summary of test conditions

	CRU filling parameters			Fuel film parameters
	Pressure (P, bar absolute)	N_2 (χ_{N_2})	O_2 (χ_{O_2})	
Test 1	2	0.79	0.21	Volume: 30 μL Thickness: 170 μm Plate temperature: 45 °C CRU temperature: 50 °C
Test 2	3	0.79	0.21	
Test 3	4	0.79	0.21	
Test 4	5	0.79	0.21	
Test 5	3	0.84	0.16	
Test 6	3	0.75	0.25	
Test 7	3	0.70	0.30	

2.2. Data processing

Although an engineered diffuser was used in the present DBIEI setup to create an extended Lambertian illumination source, the incident light intensity captured by the camera was not in any way uniform, as can be seen from the ensemble-averaged image of $I_0 - I_{BG}$ shown in Fig. 2(a). This was caused by the relatively small diameter of the optical access window of the CRU compared to the dimension of the camera's field of view. Areas with poor illumination were subject to high intensity fluctuations, as shown by the distribution of relative standard deviation in Fig. 2(b); here, the relative standard deviation for each pixel is calculated as the ratio of the standard deviation to the mean value of its intensity. The fluctuation was mainly due to the random noise of the camera. Note that the majority of the poorly illuminated area had a relative standard deviation over 0.1, while the relative standard deviation in central well-lit region remained below 0.03. Fluctuations caused by camera noise could potentially lead to uncertainties in the measured KL values; for example, a noise-induced deviation of 10% from the mean intensity would lead to a KL value of 0.11. To limit the impact of camera noise on the KL results, a threshold of 0.03 in terms of relative standard deviation was adopted to select the region of interest (ROI), which is shown in Fig. 2(b) as the area enclosed by the dashed line. It is worth pointing out that the small low-fluctuation region at the bottom of the image was the surface of the fuel plate and therefore excluded from the ROI.

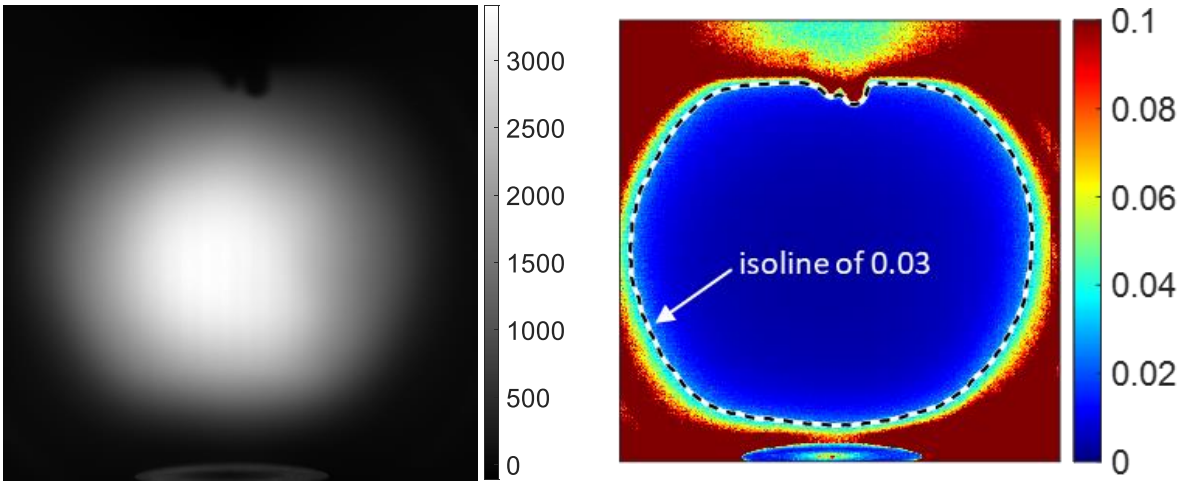

(a) Ensemble-averaged image of $I_0 - I_{BG}$ (b) Relative standard deviation of $I_0 - I_{BG}$

Fig. 2 Ensemble average and relative standard deviation of $I_0 - I_{BG}$ obtained from 100 pairs of I_0 and I_{BG} images. Dashed line marks the edge of the region of interest (ROI).

To characterise the effectiveness of this ROI, a pair of instantaneous I_0 and I_{BG} images were used

as I and I_f images in equation (2) respectively to calculate the KL distribution and the results are presented in Fig. 3; note that the I_0 and I_{BG} in the denominator of equation (2) are ensemble-averaged images. In principle, the calculated KL values should be 0 due to the absence of any flame. As shown in Fig. 3, the KL results in the ROI are significantly lower than those outside the ROI; more quantitively, the KL has a maximum value of 0.103 and a mean value of 0.003 within the ROI, which are only 4% of the corresponding values outside the ROI. Therefore, this ROI was applied to the processing of all DBIEI images, *i.e.*, all the pixels outside the ROI were excluded from KL calculation and the subsequent data processing.

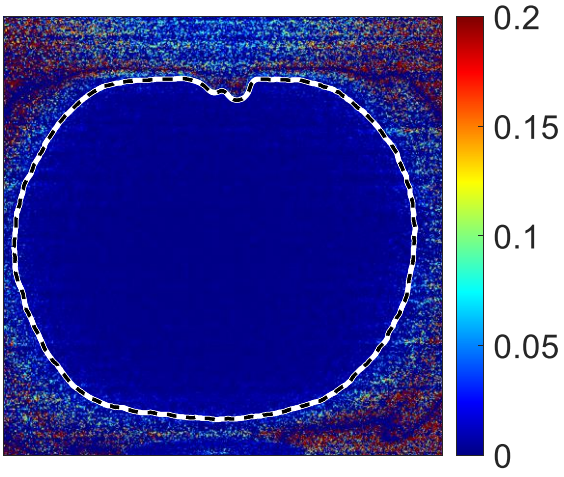

Fig. 3 KL factor calculated using a pair of instantaneous I_0 and I_{BG} images as I and I_f images respectively. Dashed line marks the edge of the ROI.

For each instantaneous spatial distribution of the KL, a spatially averaged KL factor (KL_{avg}), as an indicator of the total amount of soot present in the ROI, was calculated as follows

$$KL_{avg} = \frac{\sum_x \sum_y KL(x,y)A(x,y)}{\sum_x \sum_y A(x,y)} \tag{3}$$

where (x, y) is the coordinate of a pixel, and $KL(x, y)$ and $A(x, y)$ are the KL factor and area of a given pixel respectively. In addition, the KL-weighted centroid of the ROI was obtained to characterise how soot was distributed within the ROI, and its coordinate was calculated as:

$$x_{centroid} = \frac{\sum_x \sum_y xKL(x,y)}{\sum_x \sum_y KL(x,y)} \tag{4}$$

$$y_{centroid} = \frac{\sum_x \sum_y yKL(x,y)}{\sum_x \sum_y KL(x,y)} \tag{5}$$

The geometric centroid of the ROI was then used as a reference to evaluate the temporal movement of the KL-weighted centroid.

As will be presented in the next section, the fuel film flame showed a flickering behaviour under

many conditions tested in this study, which led to fluctuations in the total amount of soot present in the ROI. To characterise these fluctuations, temporal evolutions of the spatially averaged KL factor at three different stages, namely 1 – 2 s, 2 – 3 s and 3 – 4 s after the ignition laser pulse, were analysed using FFT (fast Fourier transform) in the frequency domain to obtain the power spectra. Each power spectrum was calculated with 512 data points and a sampling frequency of 500 Hz. It is worth noting that, within these three stages, the overall trend of KL_{avg} was to increase with time, since soot was continuously generated through fuel film combustion. Therefore, to extract the fluctuation component from the data for the calculation of power spectrum, the overall trend of each set of data was evaluated by applying a median filter with a size of 150, which was then subtracted from the original data. For each test condition, results from this processing (*i.e.*, temporal evolutions of spatially averaged KL and KL-weighted centroid, and power spectra at three different stages) were averaged across 5 measurements to obtain the ensemble-averaged values.

3. Results and discussion

3.1. Impact of ambient pressure

Fig. 4 presents some instantaneous KL spatial distributions obtained with different ambient pressures but the same ambient oxygen content, *i.e.*, χ_{O_2}= 0.21; note that all images are displayed with the same false colour scale and in sequential order with a timestep of 20 ms. As expected, the flame base was always attached to the fuel plate, regardless of the test condition. However, the flame appearance changed with time. For example, within the period of 100 ms from 2032 to 2132 ms for test 1 (P = 2 bar, χ_{O_2}= 0.21), the flame gradually grew in height and reached the top of the combustion chamber with high soot concentration in the top part of the flame; then, the flame top pinched off and the flame returned to a state similar to that at 2032 ms. A similar process was observed in the following period of 100 ms, as shown in Fig. 4(a), indicating the periodic nature of this process. This behaviour, often referred to as 'flickering' or 'puffing' in the literature, is typical for buoyant diffusion flames such as pool fires and low Reynolds number diffusion flames (Cetegen & Ahmed, 1993; Cetegen & Dong, 2000; Chamberlin & Rose, 1948; Lingens *et al.*, 1996; Xia & Zhang, 2018). The flickering behaviour results from the formation and convection of toroidal vortical structures (often referred to as the 'vortex rings'), which are formed outside the flame sheet due to the buoyancy-induced Kelvin-Helmholtz instability; this instability arises from the fact that the hot combustion-produced gas, with a low density, is accelerated by buoyancy,

resulting in shear between itself and the relatively slow flow of the ambient gas (Carpio *et al.*, 2012; L.-D. Chen *et al.*, 1989; Papadopoulos *et al.*, 2002). The flickering frequency (f) of the flame has been reported to be inversely proportional to the square root of diameter (D) of the fuel port or the fuel pool, *i.e.*,

$$f \propto D^{-\frac{1}{2}} \tag{6}$$

and typically have a value in the range of 10 – 20 Hz for most laboratory diffusion flames (Lingens *et al.*, 1996; Shaddix *et al.*, 1994). The first image for each test condition in Fig. 4 is selected in that it shows an instance just after the flame top pinched off from the flame base.

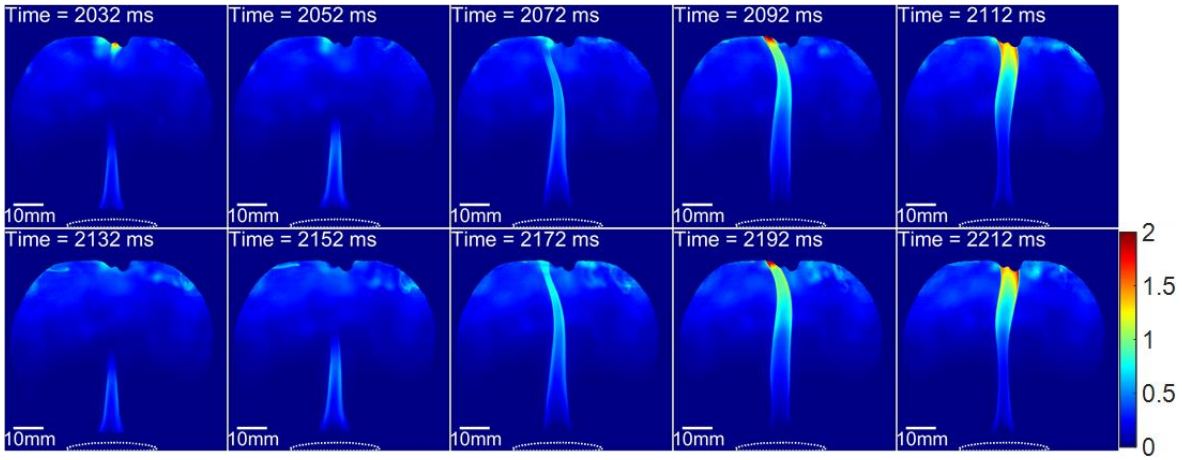

(a) Test 1, P = 2 bar, χ_{O_2} = 0.21

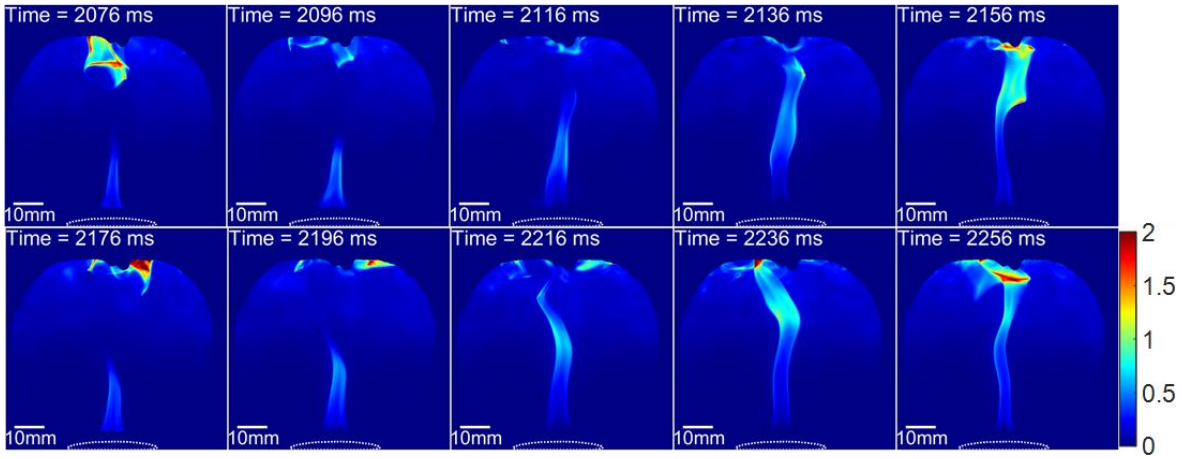

(b) Test 2, P = 3 bar, χ_{O_2} = 0.21

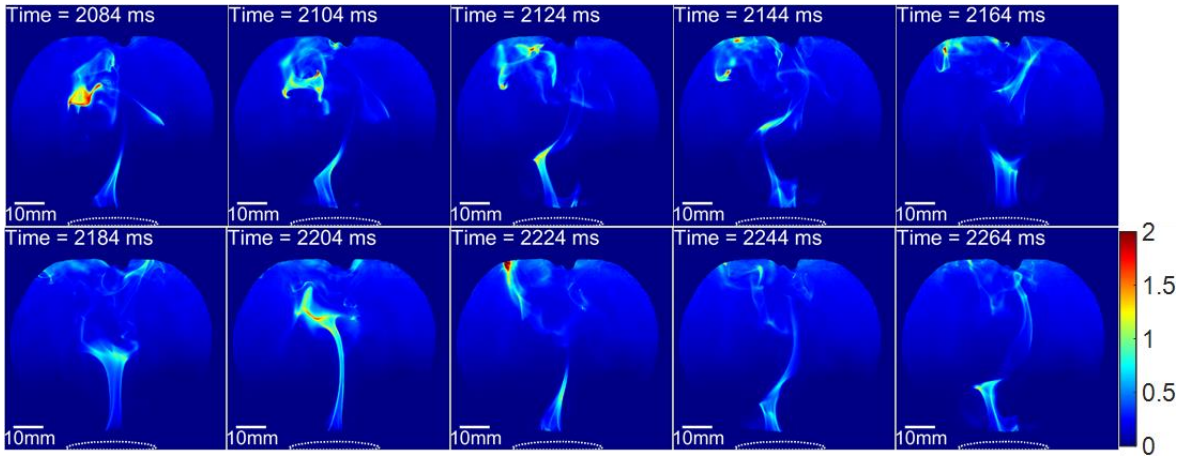

(c) Test 3, P = 4 bar, χ_{O_2} = 0.21

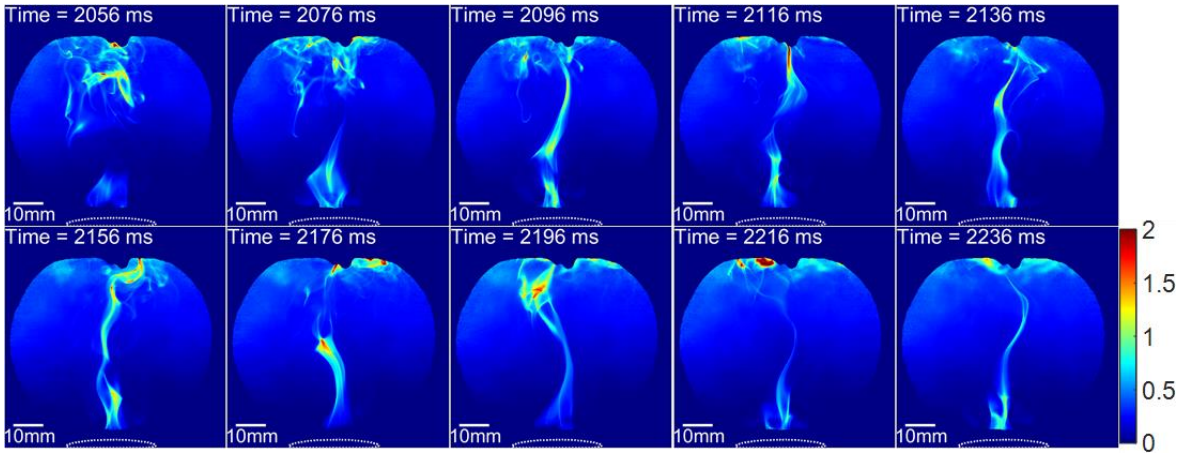

(d) Test 4, P = 5 bar, χ_{O_2} = 0.21

Fig. 4 Instantaneous spatial distributions of soot KL factor in the combustion of iso-octane fuel film within different ambient pressures and ambient oxygen content of 21%. Timestamp: delay to the ignition laser spark; dashed line: outline of fuel plate.

Flame flickering was also clearly present for P = 3 bar, as shown in Fig. 4(b). However, compared to P = 2 bar, the flame, particularly near the top and the part that pinched off, appeared wrinkled, indicating perhaps the presence of turbulent-like flow. This trend continued to develop, *i.e.*, the flame became increasingly 'turbulent', as the ambient pressure increased to 4 and 5 bar; this led to the flame flickering behaviour becoming less distinct, as shown in Fig. 4(c) and (d). A similar impact of ambient pressure on flame appearance of pool fires has been reported for ambient pressures above atmospheric pressure (J. Chen *et al.*, 2018, 2021; Most *et al.*, 1996). This impact is due to the enhancement of buoyancy at higher ambient pressures. The flame structure of pool fires is associated with the *Grashof* number (Gr), which characterises the ratio of buoyancy to viscous force as

$$Gr = \frac{g\beta\rho^2 l^3}{\mu^2}(T_f - T_\infty) \quad (7)$$

where g is the gravitational acceleration, β thermal expansion coefficient, ρ density, l characteristic length, μ dynamic viscosity, T_f flame temperature and T_∞ temperature of ambient gas (Bergman *et al.*, 2011; J. Chen *et al.*, 2018, 2021). Combining with the state equation of ideal gas ($P \propto \rho$), equation (7) leads to $Gr \propto P^2$; therefore, as ambient pressure increases, the relative magnitude of buoyancy to viscous force rises, resulting in the transition of flame appearance from laminar towards 'turbulent'.

Fig. 5 plots the temporal evolution of spatially averaged KL factor for the fuel film combustion within different ambient pressures. Several distinct features can be observed from the results. Firstly, the temporal trace of spatially averaged KL factor, which is an indicator of the total amount of soot present in the chamber, followed a similar overall trend regardless of the ambient pressure. It started to increase shortly after the fuel film was ignited, then entered a stage (1 to 4 seconds after ignition) characterised by approximately constant growth rate, after which the growth rate began to slow down and the total amount of soot gradually levelled off between 4 and 5 seconds after ignition; these three stages can be associated with the flame initiation, steady burning and flame extinction of the combustion of a fuel film, respectively. Secondly, during the steady burning stage, the total amount of soot in the chamber for P = 2 and 3 bar clearly showed a component of periodic fluctuation, which can be related to the flame flickering discussed above; consequently, since flame flickering became weaker for P = 4 and 5 bar, the periodic fluctuations in spatially averaged KL factor also appeared less marked for these two test conditions. Thirdly, there is no significant difference in the spatially averaged KL factor across different ambient pressures during the flame initiation and steady burning stages. However, this is not the case for the value where the spatially averaged KL factor eventually levelled off, *i.e.*, the total amount of soot accumulated in the chamber after flame extinguished; similar level-off value was obtained between P = 2 and 5 bar, and between P = 3 and 4 bar, while the latter value was higher than the former. This suggests that the level-off value first increased with ambient pressure, peaked between 3 and 4 bar and then decreased with ambient pressure. The increase of soot formation as ambient pressure was increased from 2 to 3 bar has also been reported by Most *et al.* (1996) and Chen *et al.* (2021), which was attributed to the fact that increasing pressure enhances soot-formation reaction rate, as suggested by Glassman (1998) or, in other words, reduces soot formation time. This *positive* correlation between ambient pressure and soot formation was also reported up to P = 5 bar by Chen *et al.* (2018), while a *negative* one was observed in this study for P > 4 bar. This may be explained by the fact that the flame for P > 4 bar in this study was significantly more 'turbulent' than that in the study by Chen *et al.* (2018); increased turbulence not only enhances the mixing

between the fuel vapour and the entrained air, but also shortens the residence times, both of which tend to reduce soot formation (Most *et al.*, 1996). Therefore, the overall effect of increasing pressure on soot formation is the combination of a) enhanced soot-formation reaction rate and b) better mixing and shorter residence times.

The spatial distribution of soot within the ROI is characterised using the KL-weighted centroid, and its temporal movement relative to the geometric centroid of the ROI is presented in Fig. 6. In the horizontal direction, the KL-weighted centroid fluctuated around the geometric centroid within a range of ±2 mm, regardless of the ambient pressure, indicating the symmetry of soot spatial distribution in this direction. The temporal movement of the KL-weighted centroid in the vertical direction, however, was drastically different. Shortly after ignition, there was a rapid movement of the KL-weighted centroid below the geometric centroid, which was due to the initial flame being short. As the flame length grew, the KL-weighted centroid soon moved to about 10 mm above the geometric centroid and stayed there during the steady burning stage despite the fluctuations in its height; this is because flames that pinched off were highly sooty, which, after impinging on the top wall of the CRU, accumulated to form a cloud of soot particles floating near the top of the chamber, as shown in Fig. 4. The fluctuations in the vertical soot distribution were closely associated with the flame flickering, since the flame flickering was mainly in the vertical direction; consequently, the fluctuations were clearly periodic for P = 2 and 3 bar, while being less so for P = 4 and 5 bar. From the flame extinction stage onward, *i.e.*, from 4 s after ignition, the soot formation gradually ceased and the soot particles – which were floating near the top of the chamber – gradually dropped due to gravity, leading to a gradual decrease in the height of the KL-weighted centroid.

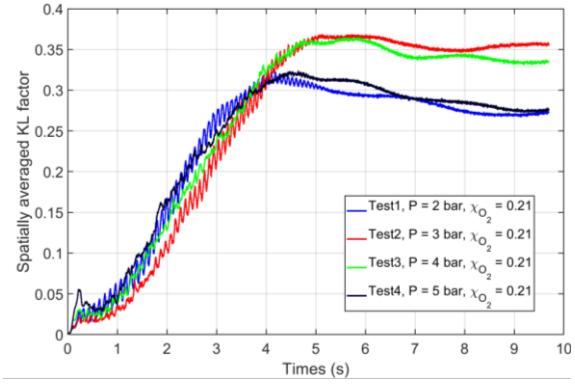

Fig. 5 Temporal evolution of spatially averaged KL factor in the combustion of iso-octane fuel film within different ambient pressures and ambient oxygen content of 21%

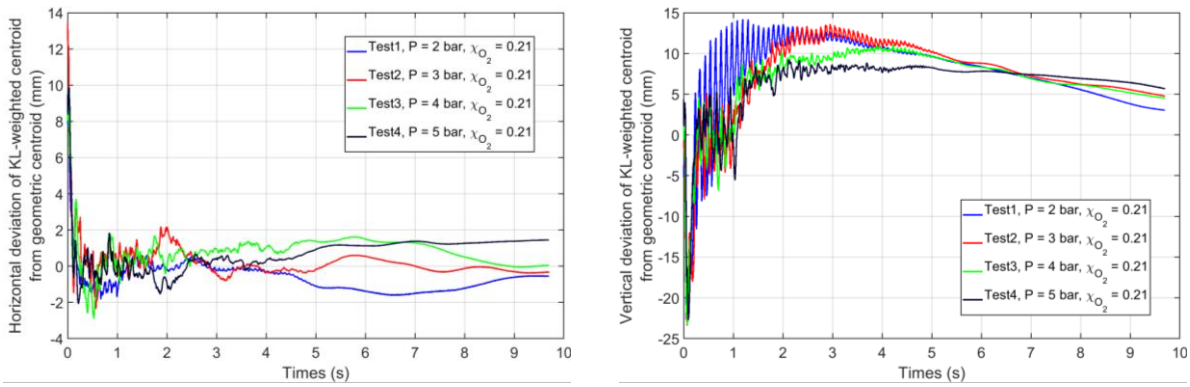

(a) Horizontal (b) Vertical

Fig. 6 Temporal movement of KL-weighted centroid relative to the geometric centroid of the ROI in the combustion of iso-octane fuel film within different ambient pressures and ambient oxygen content of 21%. Positive and negative values indicate the KL-weighted centroid is located to the right (above) and left (below) the geometric centroid respectively in the horizontal (vertical) direction.

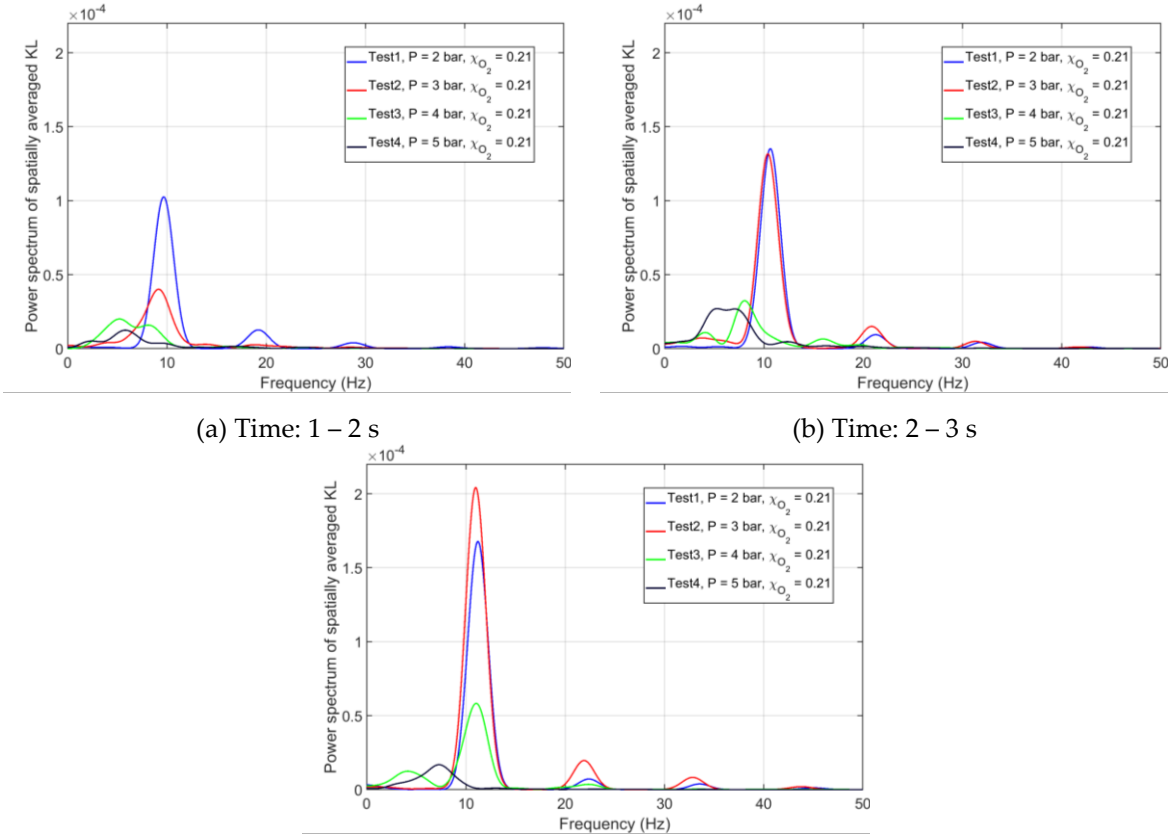

(a) Time: 1 – 2 s (b) Time: 2 – 3 s

(c) Time: 3 – 4 s

Fig. 7 Powe spectra of the spatially averaged KL factor at different stages of iso-octane fuel film combustion within different ambient pressures and ambient oxygen content of 21%

Fig. 7 presents the power spectra of the spatially averaged KL factor calculated for 3 sub-stages of the steady burning stage. It was found that for all three sub-stages, the power of the peak frequency for P = 2 and 3 bar was significantly larger than that for P = 4 and 5 bar, which agrees with the observations regarding flame flickering in Fig. 4. The peak frequencies for P = 2 and 3 bar remained at approximately 10 Hz throughout the steady burning stage, in agreement with the typical flickering frequencies (10 – 20 Hz) for most laboratory diffusion flames suggested in the literatures (Lingens *et al.*, 1996; Shaddix *et al.*, 1994). In addition, the peak frequency showed a gradual, though slight, shift towards a higher value with time for both P = 2 and 3 bar during the steady burning stage; for example, the peak frequency for P = 2 bar increased from 9.65 Hz at 1 – 2 s to 11.23 Hz at 3 – 4 s. Given the relationship shown in equation (6), this frequency shift suggests that the diameter of the fuel film gradually decreased during this stage. It is also worth noting that the power of the peak frequency clearly increased with time for both P = 2 and 3 bar during the steady burning stage. The possible reason is that as combustion proceeded, the temperature of the chamber wall and the fuel plate increased due to the continuous heat transfer (including radiative, convective and conductive) from the flame and hot combustion products, leading to enhanced vaporization of the liquid fuel and consequently, without any significant improvement in the air entrainment, relatively worsened mixing, which resulted in higher soot concentration in the flame; sootier flames, when flickering, caused higher fluctuations in the total amount of soot in the chamber. Interestingly, the power spectrum for P = 4 bar showed a more dominant peak (in other words, more distinct flame flickering) at the late steady burning stage, *i.e.*, 3 – 4 s, in comparison with earlier sub-stages, suggesting a possible influence of fuel film diameter on the flame flickering behaviour; this requires further investigation.

3.2. Impact of ambient oxygen content

Fig. 8 displays some instantaneous spatial distributions of soot KL factor obtained with different ambient oxygen contents while the ambient pressure was kept at 3 bar. Note that the same false colour scale is used in Fig. 4 and Fig. 8 to facilitate comparison. As in Fig. 4, the first image for each sequence represents an instance at which the flame top had just pinched off. It is found that when ambient oxygen content was increased above the atmospheric level (*i.e.*, $\chi_{O_2} > 0.21$), flame flickering remained distinctly observable, as shown in Fig. 8(b) and (c). In addition, soot formation in the flame was significantly enhanced. The magnitude of the soot KL factor in both the flame that pinched off, and the flame that consistently attached to the fuel film, increased with ambient oxygen content; as a result, the soot concentration in the soot cloud floating near the top of the

chamber was also substantially higher at increased ambient oxygen content. This is also quantitatively reflected in Fig. 9, where the spatially averaged KL factor is plotted as a function of time for different ambient oxygen contents. For test 7 with χ_{O_2} = 0.30, the soot production was enhanced to such a level that large chunks/clusters of soot particles were formed which floated in the chamber, as can be clearly seen in Fig. 8(c). Higher ambient oxygen content is usually expected to accelerate the soot oxidation and hence reduce the soot production in the flame, which is the opposite of the results presented here. This discrepancy could be attributed to the fact that flame temperature increased with ambient oxygen content (Glassman, 2008). Higher flame temperature accelerates the liquid fuel evaporation, which, without any significant improvement in the air entrainment, leads to increased soot formation; in addition, higher soot content in the flame increases the radiative heat transfer from the flame to the fuel film and fuel plate, thereby enhancing the fuel evaporation even further. Due to the similarity in the flame flickering behaviour among χ_{O_2} = 0.21, 0.25 and 0.30, the spatial distributions of soot within the ROI were also similar to each other, as shown in Fig. 10 by the temporal movement of the KL-weighted centroid. Additionally, periodic fluctuations were present for all three conditions in the temporal evolutions of spatially averaged KL factor and vertical height of the KL-weighted centroid during the steady burning stage.

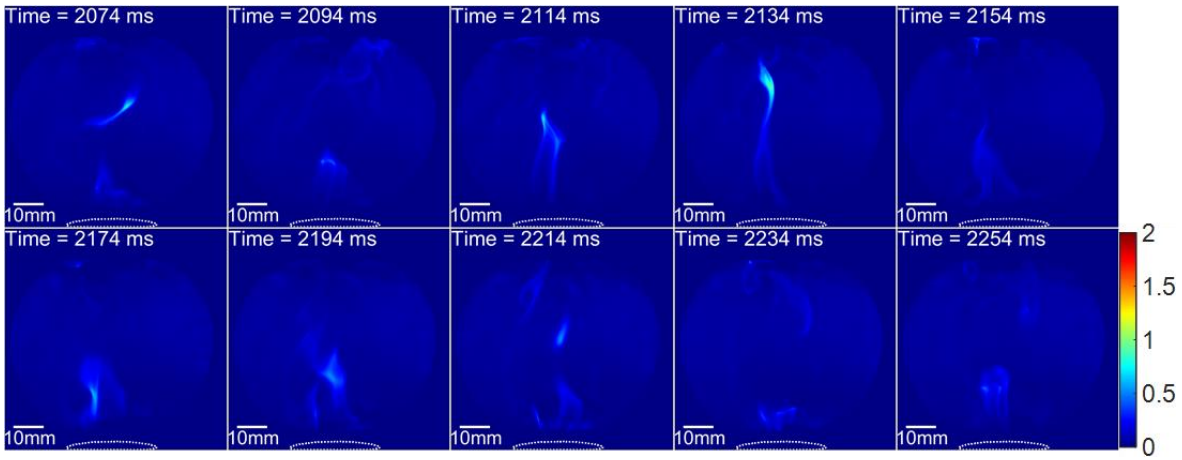

(a) Test 5, P = 3 bar, χ_{O_2} = 0.16

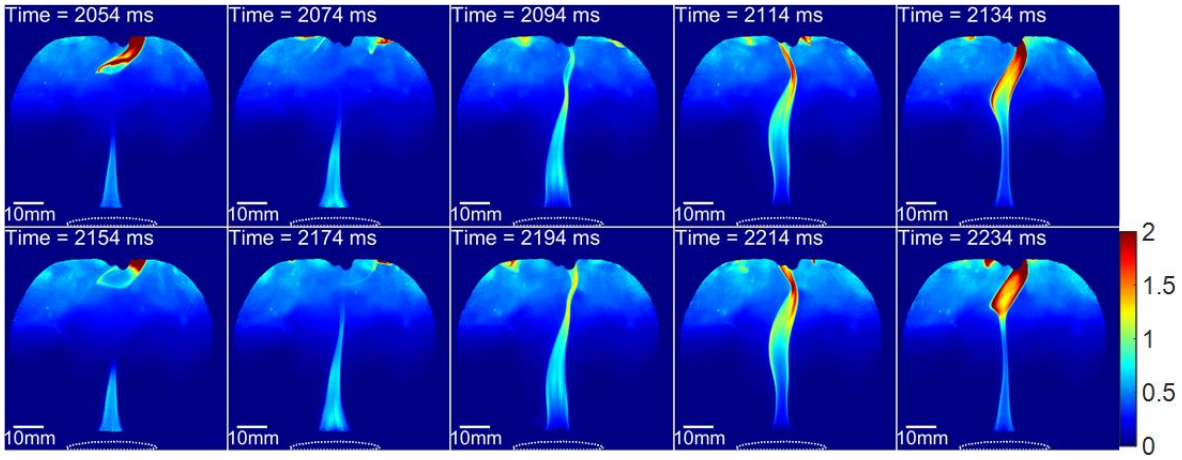

(b) Test 6, P = 3 bar, χ_{O_2} = 0.25

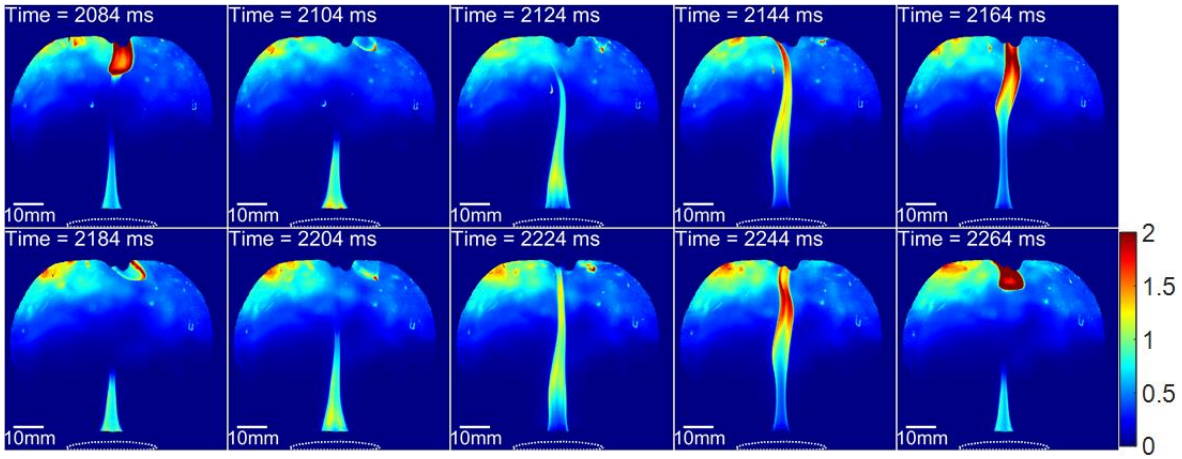

(c) Test 7, P = 3 bar, χ_{O_2} = 0.30

Fig. 8 Instantaneous spatial distributions of soot KL factor in the combustion of iso-octane fuel film within ambient pressure of 3 bar and different ambient oxygen contents. Timestamp: delay to the ignition laser spark; dashed line: outline of fuel plate.

When the ambient oxygen content was decreased below the atmospheric level, *i.e.*, χ_{O_2}= 0.16, soot formation in the flame was significantly reduced, as can be seen from both the instantaneous KL images in Fig. 8(a) and the spatially averaged KL factor in Fig. 9. This, again, might be related to changes in the flame temperature. The decreased flame temperature at lower χ_{O_2} decelerated fuel film evaporation, contributing to better mixing of the fuel vapour and entrained air before combustion reactions started; in addition, buoyancy also dropped as flame temperature reduced, which led to longer residence time and therefore enhanced oxidation of soot particles in the flame. However, the flame for χ_{O_2}= 0.16 was found to be 'turbulent', as shown in Fig. 8(a), and consequently did not have a clear flame flickering behaviour, similar to what was observed for χ_{O_2} = 0.21 with P = 4 and 5 bar. This 'turbulent' appearance of the flame at reduced ambient oxygen

content – therefore reduced flame temperature and buoyancy – was unexpected, and the causes remain unclear and require further investigation. Despite the 'turbulent' flame appearance for χ_{O_2}= 0.16, the spatial distribution of soot within the chamber for this condition was significantly different from that for χ_{O_2} = 0.21 with P = 4 and 5 bar. As shown in Fig. 10, the KL-weighted centroid remained vertically closer to the geometric centroid for χ_{O_2}= 0.16 compared with other conditions, indicating a relatively more homogeneous spatial distribution of soot; this may be attributed partly to significantly reduced soot formation, and partly to the fact that the flame appeared wider, shorter, 'turbulent' and with no distinct flame flickering, which hindered the formation of the soot cloud floating near the chamber top, as shown in Fig. 8(a).

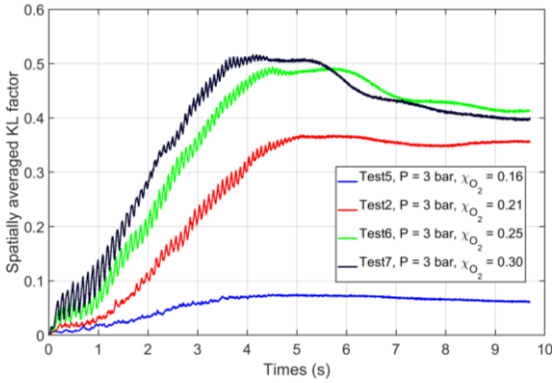

Fig. 9 Temporal evolution of spatially averaged KL factor in the combustion of iso-octane fuel film within ambient pressure of 3 bar and different ambient oxygen contents

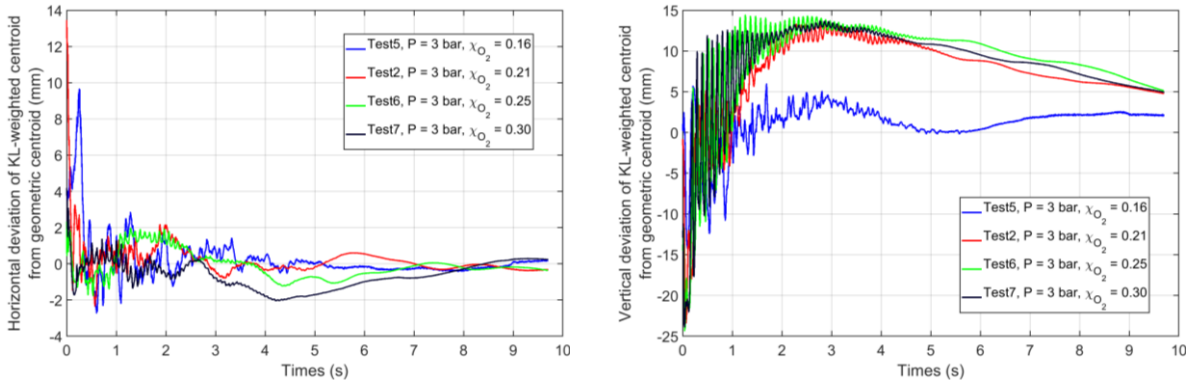

(a) Horizontal (b) Vertical

Fig. 10 Temporal movement of KL-weighted centroid relative to the geometric centroid of the ROI in the combustion of iso-octane fuel film within ambient pressure of 3 bar and different ambient oxygen contents. Definition of positive and negative same as in Fig. 6.

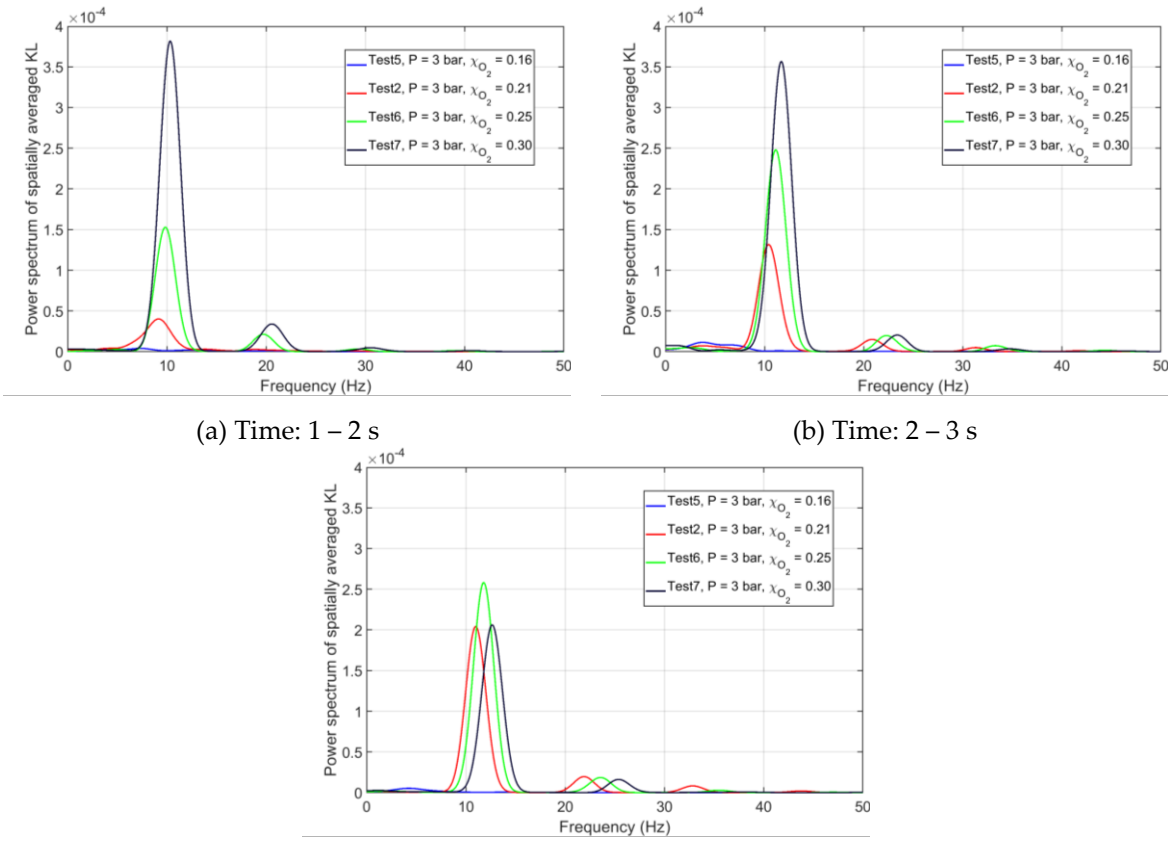

(a) Time: 1 – 2 s

(b) Time: 2 – 3 s

(c) Time: 3 – 4 s

Fig. 11 Power spectra of the spatially averaged KL factor at different stages of iso-octane fuel film combustion within different ambient pressures and ambient oxygen content of 21%

Power spectra of the spatially averaged KL factor were calculated at three sub-stages of the steady burning stage for different ambient oxygen contents and the results are presented in Fig. 11. It is found that there was no clear peak in the spectrum for χ_{O_2}= 0.16 throughout the steady burning stage, while the spectra for higher χ_{O_2} showed strong peaks at approximately 10 Hz, which agrees with the observations regarding flame flickering in Fig. 8. The shift of peak frequency towards higher values with time was also observed for χ_{O_2} = 0.25 and 0.30, again suggesting the shrinkage of the fuel film diameter during the steady burning stage. In terms of the power of the peak frequency, a positive correlation with the ambient oxygen content was found at the beginning of the steady burning stage, *i.e.*, 1 – 2 s, which was related to the enhanced soot concentration in the flame with increased ambient oxygen content. As combustion proceeded, the power of the peak frequency gradually increased for χ_{O_2}= 0.21 and decreased for χ_{O_2}=0.30, while first increased then stabilized for χ_{O_2} = 0.25. The increase for χ_{O_2}= 0.21 has been discussed in the previous section and attributed to the flame becoming sootier with time. The decrease for χ_{O_2}= 0.30, on the other hand, can be associated with the rapid fuel consumption during the steady burning stage due to the

increased flame temperature. Fuel consumption led to reduced fuel film diameter and therefore smaller flame volume, which resulted in weaker fluctuations in the total amount of soot within the chamber, since the size of the flame tip that pinched off reduced. The trend in the case of χ_{O_2} = 0.30 can be explained by the competition between these two effects, *i.e.*, flame becoming sootier and smaller.

4. Conclusions

In the context of pool fires in GDI engines, we investigated the combustion of liquid iso-octane films without extraneous effects from simultaneous combustion of the injected spray by using a custom-made liquid fuel film generation system. Using laser-induced spark ignition within a constant volume chamber filled with N_2/O_2 mixtures, the ambient pressure and molar fraction of O_2 were varied over 2 – 5 bar absolute and 16 – 30% respectively. To examine their impact on flame appearance and soot formation from combustion of the fuel film, we performed visualisation at high temporal and spatial resolution using the high-speed DBIEI technique. Temporal evolution of the total amount of soot and spatial distribution of soot within the chamber, characterized by the spatially averaged soot optical thickness (KL factor) and KL-weighted centroid respectively, were obtained from image processing of the instantaneous KL results. Temporal traces of the spatially averaged KL factor were further analysed in the frequency domain to extract the power spectra, thereby identifying the frequency and power of the fluctuations in the amount of soot generated from fuel film combustion. The main findings from this study are listed as follows:

(1) Flame flickering became less distinct when the fuel film flame gradually changed from laminar to more turbulent in appearance as the ambient pressure was increased and/or the ambient oxygen content was reduced below the atmospheric level.

(2) Flame flickering led to periodic fluctuations in the spatially averaged KL factors, at a frequency of approximately 10 Hz for the conditions examined which gradually increased with time as the diameter of the fuel film reduced. The temporal change of the fluctuation power showed dependency on the test condition, which was associated with the temporal variations of the soot concentration and volume of the flames.

(3) The overall soot formation during fuel film combustion first increased then decreased with ambient pressure, with a peak occurring between 3 and 4 bar. This is attributed to the fact that higher ambient pressure resulted in both increased soot-formation reaction rate and better mixing of fuel vapour with entrained air, which counteracted each other in terms of soot formation. Increased ambient oxygen content was found to enhance soot formation,

mainly due to its positive effect on flame temperature and consequently on fuel evaporation rate.

(4) The spatial distribution of soot within the chamber was relatively symmetrical in the horizontal direction throughout the combustion, regardless of the test condition. The distribution in the vertical direction, however, was significantly skewed towards the top of the chamber shortly after the flame was established, due to the formation of a soot cloud floating near the chamber top resulting from flame flickering and buoyancy effects.

Acknowledgements

The authors would like to acknowledge the financial support from the Engineering and Physical Sciences Research Council (EPSRC) through grant EP/V027050/1. Messrs Colin Hall and Asanka Munasinghe provided invaluable assistance with the construction of the CRU and the fuel film generation system, and of the DBIEI's LED electronics, respectively.

References

Bergman, T. L., Bergman, T. L., Incropera, F. P., DeWitt, D. P., & Lavine, A. S. (2011). *Fundamentals of Heat and Mass Transfer*. John Wiley & Sons.

Bjørgen, K. O. P., Emberson, D. R., & Lovas, T. (2019). Diffuse Back-Illuminated Extinction Imaging of Soot: Effects of Beam Steering and Flame Luminosity. *SAE International Journal of Engines*, *1*. https://doi.org/10.4271/2019-01-0011

Carpio, J., Sánchez-Sanz, M., & Fernández-Tarrazo, E. (2012). Pinch-off in forced and non-forced, buoyant laminar jet diffusion flames. *Combustion and Flame*, *159*(1), 161–169. https://doi.org/10.1016/j.combustflame.2011.06.008

Cetegen, B. M., & Ahmed, T. A. (1993). Experiments on the periodic instability of buoyant plumes and pool fires. *Combustion and Flame*, *93*(1), 157–184. https://doi.org/10.1016/0010-2180(93)90090-P

Cetegen, B. M., & Dong, Y. (2000). Experiments on the instability modes of buoyant diffusion flames and effects of ambient atmosphere on the instabilities. *Experiments in Fluids*, *28*(6), 546–558. https://doi.org/10.1007/s003480050415

Chamberlin, D. S., & Rose, A. (1948). The flicker of luminous flames. *Proceedings of the Symposium on Combustion*, *1–2*, 27–32. https://doi.org/10.1016/S1062-2888(65)80007-7

Chen, J., Zhao, Y., Bi, Y., Li, C., Kong, D., & Lu, S. (2021). Effect of initial pressure on the burning behavior of ethanol pool fire in the closed pressure vessel. *Process Safety and Environmental Protection*, *153*, 159–166. https://doi.org/10.1016/j.psep.2021.07.022

Chen, J., Zhao, Y., Chen, X., Li, C., & Lu, S. (2018). Effect of pressure on the heat transfer and flame characteristics of small-scale ethanol pool fires. *Fire Safety Journal*, *99*, 27–37. https://doi.org/10.1016/j.firesaf.2018.06.001

Chen, L.-D., Seaba, J. P., Roquemore, W. M., & Goss, L. P. (1989). Buoyant diffusion flames. *Symposium (International) on Combustion*, *22*(1), 677–684. https://doi.org/10.1016/S0082-0784(89)80075-X

Chung, J., Kim, W., Kim, J., Min, K., & Lee, J. (2021). *The Effects of Fuel Film on Soot Formation of GDI Injector using Optical Diagnostics*. *1*.

Ding, C.-P., Sjöberg, M., Vuilleumier, D., Reuss, D. L., He, X., & Böhm, B. (2018). Fuel film thickness measurements using refractive index matching in a stratified-charge SI engine operated on E30 and alkylate fuels. *Experiments in Fluids*, *59*(3). https://doi.org/10.1007/s00348-018-2512-5

Drake, M. C., Fansler, T. D., Solomon, A. S., & Szekely, G. A. (2003). Piston Fuel Films as a Source of Smoke and Hydrocarbon Emissions from a Wall-Controlled Spark-Ignited Direct-Injection Engine. *SAE Transactions*, *112*, 762–783. JSTOR.

Duke, D. J., Swantek, A. B., Sovis, N. M., Tilocco, F. Z., Powell, C. F., Kastengren, A. L., Gürsoy, D., & Biçer, T. (2016). Time-resolved X-ray Tomography of Gasoline Direct Injection Sprays. *SAE International Journal of Engines*, *9*(1), 143–153. https://doi.org/10.4271/2015-01-1873

Glassman, I. (1998). Sooting laminar diffusion flames: Effect of dilution, additives, pressure, and microgravity. *Symposium (International) on Combustion*, *27*(1), 1589–1596. https://doi.org/10.1016/S0082-0784(98)80568-7

Glassman, I. (2008). *Combustion* (4th ed.). Academic.

He, X., Li, Y., Sjöberg, M., Vuilleumier, D., Ding, C.-P., Liu, F., & Li, X. (2019). Impact of coolant temperature on piston wall-wetting and smoke generation in a stratified-charge DISI engine operated on E30 fuel. *Proceedings of the Combustion Institute*, *37*(4), 4955–4963. https://doi.org/10.1016/j.proci.2018.07.073

Hua, X. (2021). *Jet and Spray Characteristics in Advanced Compression Ignition Engines* [PhD]. Imperial College London.

Jüngst, N., & Kaiser, S. (2019). *Imaging of Fuel-Film Evaporation and Combustion in a Direct-Injection Model Experiment*. SAE Technical Paper Series. https://doi.org/10.4271/2019-01-0293

Jüngst, N., & Kaiser, S. A. (2021). Visualization of soot formation from evaporating fuel films by laser-induced fluorescence and incandescence. *Proceedings of the Combustion Institute*, *38*(1), 1089–1097. https://doi.org/10.1016/j.proci.2020.06.076

Karlsson, R. B., & Heywood, J. B. (2001). Piston Fuel Film Observations in an Optical Access GDI Engine. *SAE Transactions*, *110*, 1505–1516. JSTOR.

Lind, T., Roberts, G., Eagle, W., Rousselle, C., Andersson, Ö., & Musculus, M. P. B. (2018). *Mechanisms of Post-Injection Soot-Reduction Revealed by Visible and Diffused Back-Illumination Soot Extinction Imaging*. *1*. https://doi.org/10.4271/2018-01-0232

Lingens, A., Neemann, K., Meyer, J., & Schreiber, M. (1996). Instability of diffusion flames. *Symposium (International) on Combustion*, *26*(1), 1053–1061. https://doi.org/10.1016/S0082-0784(96)80319-5

Miyashita, K., Tsukamoto, T., Fukuda, Y., Kondo, K., & Aizawa, T. (2016). *High-Speed UV and Visible Laser Shadowgraphy of GDI In-Cylinder Pool Fire*. https://doi.org/10.4271/2016-01-2165

Most, J.-M., Mandin, P., Chen, J., Joulain, P., Durox, D., & Carlos Fernande-Pello, A. (1996). Influence of gravity and pressure on pool fire-type diffusion flames. *Symposium (International) on Combustion*, *26*(1), 1311–1317. https://doi.org/10.1016/S0082-0784(96)80349-3

Papadopoulos, G., Bryant, R., & Pitts, W. (2002). Flow characterization of flickering methane/air diffusion flames using particle image velocimetry. *Experiments in Fluids*, *33*(3), 472–481. https://doi.org/10.1007/s00348-002-0483-y

Phuoc, T. X. (2006). Laser-induced spark ignition fundamental and applications. *Optics and Lasers in Engineering*, *44*(5), 351–397. https://doi.org/10.1016/j.optlaseng.2005.03.008

Ronney, P. D. (1994). Laser versus conventional ignition of flames. *Optical Engineering*, *33*(2), 510–521. https://doi.org/10.1117/12.152237

Roque, A., Foucher, F., Imoehl, W., & Helie, J. (2019). *Generation and Oxidation of Soot due to Fuel Films Utilizing High Speed Visualization Techniques*. SAE Technical Paper Series. https://doi.org/10.4271/2019-01-0251

Roque, A., Foucher, F., Lamiel, Q., Imoehl, B., Lamarque, N., & Helie, J. (2019). Impact of gasoline direct injection fuel films on exhaust soot production in a model experiment. *International Journal of Engine Research*, *21*(2), 367–390. https://doi.org/10.1177/1468087419879851

Shaddix, C. R., Harrington, J. E., & Smyth, K. C. (1994). Quantitative measurements of enhanced soot production in a flickering methane/air diffusion flame. *Combustion and Flame*, *99*(3–4), 723–732. https://doi.org/10.1016/0010-2180(94)90067-1

Westlye, F. R., Penney, K., Ivarsson, A., Pickett, L. M., Manin, J., & Skeen, S. A. (2017). Diffuse back-illumination setup for high temporally resolved extinction imaging. *Appl Opt*, *56*(17), 5028–5038. https://doi.org/10.1364/AO.56.005028

Xia, X., & Zhang, P. (2018). A vortex-dynamical scaling theory for flickering buoyant diffusion flames. *Journal of Fluid Mechanics*, *855*, 1156–1169. https://doi.org/10.1017/jfm.2018.707

Zhao, F., Lai, M. C., & Harrington, D. L. (1999). Automotive spark-ignited direct-injection gasoline engines. *Progress in Energy and Combustion Science*, *25*(5), 437–562. https://doi.org/10.1016/S0360-1285(99)00004-0

Zhao, H. (2010). *Advanced direct injection combustion engine technologies and development. Volume 1, Gasoline and gas engines*. CRC Press.